

Three-dimensional fast magnetic reconnection driven by relativistic ultraintense femtosecond lasers

Y. L. Ping,^{1,*} J. Y. Zhong,¹ Z. M. Sheng,^{2,5} X. G. Wang,³ B. Liu,⁴ Y. T. Li,⁵ X. Q. Yan,^{3,4} X. T. He,⁴ J. Zhang,^{2,5} and G. Zhao^{1,†}

¹Key Laboratory of Optical Astronomy, National Astronomical Observatories, Chinese Academy of Sciences, Beijing 100012, China

²Key Laboratory for Laser Plasmas (MOE) and Department of Physics and Astronomy, Shanghai Jiao Tong University, Shanghai 200240, China

³State Key Laboratory of Nuclear Physics and Technology, School of Physics, Peking University, Beijing 100871, China

⁴Center for Applied Physics and Technology, Peking University, Beijing 100084, China

⁵Beijing National Laboratory of Condensed Matter Physics, Institute of Physics, Chinese Academy of Sciences, Beijing 100080, China

(Received 19 July 2012; revised manuscript received 12 June 2013; published 7 March 2014)

Three-dimensional fast magnetic reconnection driven by two ultraintense femtosecond laser pulses is investigated by relativistic particle-in-cell simulation, where the two paralleled incident laser beams are shot into a near-critical plasma layer to form a magnetic reconnection configuration in self-generated magnetic fields. A reconnection X point and out-of-plane quadrupole field structures associated with magnetic reconnection are formed. The reconnection rate is found to be faster than that found in previous two-dimensional Hall magnetohydrodynamic simulations and electrostatic turbulence contribution to the reconnection electric field plays an essential role. Both in-plane and out-of-plane electron and ion accelerations up to a few MeV due to the magnetic reconnection process are also obtained.

DOI: 10.1103/PhysRevE.89.031101

PACS number(s): 52.35.Vd, 52.30.-q, 52.50.Jm, 52.65.Rr

Magnetic reconnection (MR) [1,2] occurs widely in fast energy release processes such as in solar flares [3,4], coronal mass ejections, interaction of solar and magnetosphere [5], certain explosive astrophysical events [6], and fusion plasma instabilities [7]. Moreover, the relativistic magnetic reconnection may play an important role for energy conversion in relativistic objects, for example, hard x-ray and higher energy spectrum bursts in solar flares [8], pulsars [9], gamma-ray bursts [10], and active galactic nuclei [11]. With the development of high energy and high power long lasers, there is an increasing interest to investigate this kind of process in the laboratory [12–15]. Related two-dimensional particle-in-cell (2D PIC) simulation has been carried out with preassumed laser-produced plasma bubble structures [16].

These laser-driven MR configurations were realized with magnetic fields typically at the mega-gauss (MG) level produced by nonparallel temperature and density gradients [12–15], which are located near the target surface. On the other hand, it is well known that the intensive quasistatic magnetic fields over 100 MG can be generated by the relativistic intense lasers interacting with plasma, as shown numerically [17–19] and theoretically [20–22]. Near giga-Gauss (GG) magnetic fields have been measured in intense laser interaction with solid targets, where the region of strong magnetic fields is located both at surface and inside the target [23]. Due to dynamic evolution of the magnetic fields, magnetic interaction [24] and reconnection [25] have been foreseen in such laser-produced plasmas.

In this Rapid Communication, we report a relativistic PIC simulation using KLAP code [26,27] for a three-dimensional (3D) MR process occurring in intense femtosecond laser pulse produced plasmas. Two femtosecond laser pulses, parallel to each other, are shot into a target of near critically dense plasma layer. Fast reconnection of the GG level magnetic

field inside the target is then demonstrated. Such a magnetic reconnection process can be possibly realized experimentally with subpicosecond subpetawatt intense laser systems such as LFEX [28] and OMEGA-EP [29].

The simulation is performed in a box of $L_{x0} = L_{y0} = 24 \mu\text{m}$ and $L_{z0} = 40 \mu\text{m}$, with $480 \times 480 \times 800$ cells and 10^9 quasiparticles. Two identical circularly polarized laser beams shoot at the target and then propagate in parallel in the box along the z axis. The lasers have a peak intensity of $5 \times 10^{20} \text{ W/cm}^2$ corresponding to a normalized laser vector potential $a_0 = 13.5$, a spot diameter of $3 \mu\text{m}$, the wavelength $\lambda_0 = 1 \mu\text{m}$, and the laser period $T_0 = \lambda_0/c$. The incident laser pulse has a rising front of two laser cycles followed by a flat top in the z direction and is a Gaussian form in the x, y directions. The distance between two laser centroids is $8 \mu\text{m}$. A near-critical density plasma target is located in $5 \mu\text{m} < z < 35 \mu\text{m}$ with nonuniform density in the z direction and uniform density in the x, y directions. The density linearly increases to a critical density from 5 to $10 \mu\text{m}$, and then remains constant for $10 \mu\text{m} < z < 15 \mu\text{m}$, then linearly decreases as $n = [1 - (z - z_0)/L_0]n_c$, $L_0 = 20 \mu\text{m}$ for $15 \mu\text{m} < z < 35 \mu\text{m}$, where $z_0 = 15 \mu\text{m}$. In the transverse directions, periodic boundary conditions are applied for particles and fields. Particles are reflected and fields are absorbed at the boundaries in the longitudinal direction. The temperatures of the initial ion and electron are 0.01 and 10 keV, respectively. The ions are simply protons with the mass ratio $m_p/m_e = 1836$. The critical density is $n_c = m_e \omega_0^2 / 4\pi e^2 = 1.15 \times 10^{21} \text{ cm}^{-3}$, where m_e is the electron rest mass, ω_0 represents the laser angular frequency, and e is the element charge. It has been shown by Nakamura *et al.* [30] and Bulanov *et al.* [31] that the produced magnetic fields can expand laterally when intense laser beams propagate in inhomogeneous plasmas from the higher density to the lower density or vacuum.

When an ultraintense laser propagates in underdense plasmas, both electron and ion density channels are formed. For the circularly polarized laser pulses, an axial field B_z can be generated through the inverse Faraday effect [20–22],

*ylping@bao.ac.cn

†gzhaoy@bao.ac.cn

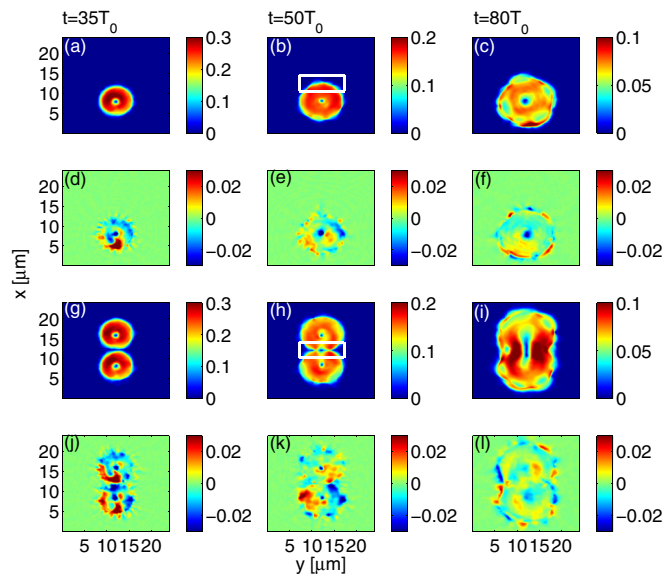


FIG. 1. (Color online) Snapshots (at $z = 20.7 \mu\text{m}$ from $35T_0$ to $80T_0$) of magnetic fields \mathbf{B} . (a)–(c) Azimuthal magnetic fields B_θ and (d)–(f) out-of-plane magnetic fields B_z produced by a single incident laser. (g)–(i) B_θ and (j)–(l) B_z by two incident lasers. Here, the magnetic fields are normalized by the initial laser field $B_0 = \sqrt{I/\epsilon c}/c = 1.45 \text{ GG}$. The region in the white line surrounded box contains a reconnection region and an outflow region.

and an azimuthal field B_θ is produced from the longitudinal current driven by the laser acceleration [32,33]. The evolution of the magnetic fields, normalized to the initial laser field $B_0 = \sqrt{I/\epsilon c}/c = 1.45 \text{ GG}$, from $35T_0$ to $80T_0$ in plasma at $z = 20.7 \mu\text{m}$ is shown in Figs. 1(g)–1(l). As a reference, the field generated by a single incident laser pulse is also plotted in Figs. 1(a)–1(f). Clearly the azimuthal magnetic field expands

laterally due to the force acting on the vortex in the $\nabla n \times \Omega$ direction [34] with its topological structure kept unchanged, as an expanding bubble with an O -point-type null at the center. The evolution of the azimuthal magnetic field produced by the two lasers is shown in Figs. 1(g)–1(i). Irradiated by the lasers, the azimuthal fields expand toward each other at $t = 35T_0$. At this moment, the magnetic fields of two bubbles do not yet meet [Fig. 1(g)]. At $t = 50T_0$, however, much of the magnetic flux is already reconnected, as shown in Fig. 1(h). The X -point-type magnetic null is then found between the two bubbles. It is the place where the magnetic field vanishes as the magnetic bubbles with different polarities meet one another, that MR occurs. As the process goes on, the two bubbles start to merge together into a single big bubble as shown in Fig. 1(i). The area with heavily diminished field strength also increases, where the magnetic energy is converted to kinetic energy of electrons and ions, forming outflow jets along the y direction and out-of-plane acceleration along the z direction, as shown in Fig. 4 later. At $t = 80T_0$, the two bubbles merge with each other completely and the new magnetic topological structure is formed.

The out-of-plane magnetic fields B_z generated by a single laser pulse and two lasers are also shown in Figs. 1(d)–1(f) and 1(j)–1(l), respectively. In the case of one laser [Fig. 1(d)–1(f)], it is found that the magnetic field structure is always nearly centrosymmetric. In the case of two lasers [Figs. 1(j)–1(l)], however, a quadrupole structure appears around the reconnection site, which is a typical signature of the Hall effect [1,35]. The reconnection process is clearly collisionless since the width of the diffusion region [$< 5 \mu\text{m}$ as shown in Fig. 3(b)] is much less than the ion skin depth. The ion skin depth is calculated as $d_i = c/\omega_{pi} \approx 8.3 \mu\text{m}$ at $z = 20.7 \mu\text{m}$, where $\omega_{pi} = (4\pi e^2 n_0/m_i)^{1/2}$ is the ion plasma frequency. However, the electron skin depth is $d_e = c/\omega_{pe} \approx 0.71 \mu\text{m}$, where the electron plasma frequency is $\omega_{pe} = (4\pi e^2 n_0/\gamma_0 m_e)^{1/2}$ with

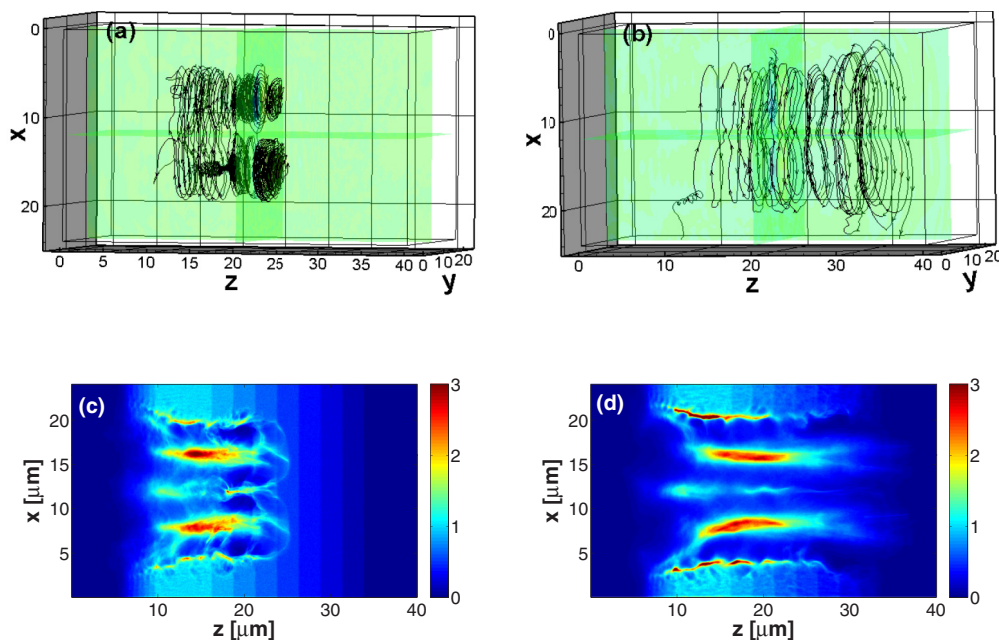


FIG. 2. (Color online) (a), (b) Snapshots of three-dimensional magnetic field lines (a) at $35T_0$ and (b) at $50T_0$. (c), (d) Corresponding electron density normalized by n_c in the x - z plane at $y = 12 \mu\text{m}$.

the relativistic factor $\gamma_0 \approx \sqrt{1 + a_0^2}$. Since the reconnection region size is less than d_i , the Hall magnetohydrodynamics (MHD) model may not be applied and the electron MHD (EMHD) model is used in the fluid approach [36]. In EMHD, the generalized vorticity should be frozen in the electron component if the plasma density is initially uniform. In the region where the displacement current effect is significant, the general vorticity of $\mathbf{\Omega}_e = -e(1 - d_e^2 \nabla^2) \mathbf{B}/c$ should be rewritten as $\mathbf{\Omega}_e = -\frac{e}{c} [1 - d_e^2 (\nabla^2 - \frac{1}{c^2} \frac{\partial^2}{\partial t^2})] \mathbf{B}$. Then the optical propagating operator of $\nabla^2 - \partial^2/c^2 \partial t^2$ can then spread the electromagnetic fluctuations, in the small scale of and below d_e , out of the reconnection region. Additionally, the nonuniformity of the plasma induces the Biermann battery effect, also called the baroclinic effect in fluid theory, of $\nabla n_e \times \nabla T_e$ to break the frozen-in condition and meanwhile to generate the magnetic field.

The 3D magnetic field configurations and corresponding electron density are plotted in Fig. 2. At $t = 35T_0$ when the laser pulses have not yet reached most of the right half of the simulation box, two magnetic flux tubes have already clearly shaped [shown in Fig. 2(a)] and the lasers transport in the plasmas in Fig. 2(c). Then, a fully developed 3D magnetic reconnection configuration is formed at $t = 50T_0$ [Fig. 2(b)] with the two flux tubes reconnecting into one in the outer region.

Figures 3(a)–3(d) show the reconnection electric field at two characteristic moments ($35T_0$ and $50T_0$). At $t = 35T_0$ reconnection has not yet fully developed and the electric field $\langle E_z \rangle$ between the bubbles is very low. As time increases the

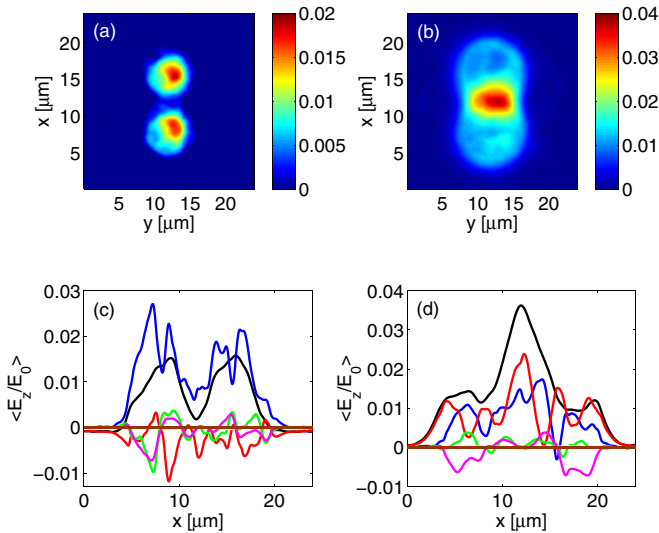


FIG. 3. (Color online) Reconnection electric field $\langle E_z \rangle$ at $t = 35T_0$ [(a), (c)] and at $t = 50T_0$ [(b), (d)]. (c), (d) Contributions of terms in the generalized Ohm's law from Eq. (1) to $\langle E_z \rangle$ (black) along the x axis at (c) and (d) for $y = 12 \mu\text{m}$, as $\frac{1}{e(n_e)} ((\mathbf{j}) \times \langle \mathbf{B} \rangle)_z$ (purple), $-\frac{1}{e(n_e)} (\nabla \cdot \mathbf{P}_e)_z$ (blue), $\frac{m_e}{e^3(n_e)} ((\mathbf{j}) \cdot \nabla (\frac{\mathbf{j}}{n_e}))$ (brown), $\frac{m_e}{(n_e)e^2} \frac{\partial (\frac{\mathbf{j}}{n_e})}{\partial t}$ (yellow), $-\frac{1}{(n_e)} \langle \delta n_e \delta E_z \rangle$ (red), and $\frac{1}{e(n_e)} \langle \delta \mathbf{j} \times \delta \mathbf{B} \rangle_z$ (green). $\langle A \rangle$ means that variable A is smoothed over the fast oscillation and then averaged over the z direction from 5 to 35 μm . Here, the electric fields is normalized by the initial laser field $E_0 = cB_0 = 4.34 \times 10^{13}$ V/m.

reconnection electric field component $\langle E_z \rangle$ at the X point starts to increase and reaches its maximum at $t = 50T_0$.

Another important parameter for MR is the reconnection rate $c \langle E_z \rangle / \langle B_A V_A \rangle$, where the mean field of a variable A , $\langle A \rangle$, is smoothed over the fast oscillation and then averaged over the z direction, and its fluctuation $\delta A = A - \langle A \rangle$, $\langle B_A \rangle$ is asymptotic magnetic field strength and $\langle V_A \rangle$ is the corresponding Alfvén speed, as $\langle V_A \rangle = \langle B_A \rangle / \sqrt{4\pi\rho}$, where $\rho = m_p n_i + m_e n_e$ is the mass density of the plasma with n_i and n_e being the ion and electron number densities, respectively. The reconnection electric field $\langle E_z \rangle$ on the line of $y = 12 \mu\text{m}$ at $35T_0$ and $50T_0$ is then plotted in Figs. 3(c) and 3(d). As shown above, at $t = 35T_0$, flux tubes have not fully formed in the simulation domain and the corresponding reconnection field near the X point $x = 12 \mu\text{m}$ are very small. At $t = 50T_0$ reconnection is proceeding throughout the box and the reconnection electric field reaches its maximum. The asymptotic Alfvén speed is $\langle V_A \rangle = 1.483 \times 10^9$ cm/s (nearly 1/20 of the speed of light in vacuum) with $\langle B_A \rangle = 0.1$ at $x = 9.75 \mu\text{m}$. The reconnection rate is then calculated to be $c \langle E_z \rangle / \langle B_A V_A \rangle = 6.72$, almost two orders of magnitude higher than the typical value 0.1 obtained by 2D MHD simulations for Hall magnetic reconnection [37]. In fact, in the short pulse laser-driven duration, the ion is approximately at rest in comparison with the electron, as shown in Fig. 4. Then the reconnection electrical field should be scaled by the electron Alfvén velocity $V_{Ae} \sim c/\sqrt{\epsilon} \approx 0.9992c$, where $\epsilon = 1 + 2(\omega_{pe}/\Omega_c)^2$ is the relative permittivity with the electron cyclotron frequency $\Omega_c = eB/m_e c$, as $c \langle E_z \rangle / \langle B_A V_{Ae} \rangle \approx 0.44$. It is still much faster than that of 2D MHD simulations, a significant feature of strong driven fast reconnection.

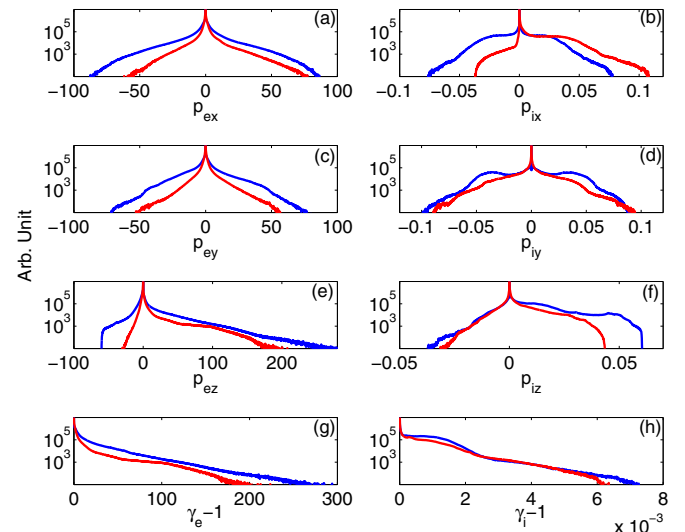


FIG. 4. (Color online) Electron momentum distributions (a) $p_{ex} = \gamma_e \beta_{ex}$, (c) $p_{ey} = \gamma_e \beta_{ey}$, and (e) $p_{ez} = \gamma_e \beta_{ez}$; ion momentum distributions (b) $p_{ix} = \gamma_i \beta_{ix}$, (d) $p_{iy} = \gamma_i \beta_{iy}$, and (f) $p_{iz} = \gamma_i \beta_{iz}$, as well as their energy distributions (g) for electrons normalized by $m_e c^2$ and (h) for ions normalized by $m_i c^2$, in the white line surrounded box ($10 \mu\text{m} < x < 14 \mu\text{m}$, $7 \mu\text{m} < y < 17 \mu\text{m}$) shown in Figs. 1(b) and 1(h) with $11 \mu\text{m} < z < 35 \mu\text{m}$ at $t = 50T_0$. The red lines are for a laser and the blue lines are for two lasers.

From the generalized Ohm's law [38,39] of the mean field, $\langle E_z \rangle$ can be written as

$$\begin{aligned} \langle E_z \rangle = & \frac{1}{e\langle n_e \rangle} (\langle \mathbf{j} \rangle \times \langle \mathbf{B} \rangle)_z + \frac{-1}{e\langle n_e \rangle} \langle \nabla \cdot \mathbf{P}_e \rangle_z \\ & + \frac{m_e}{e^3 \langle n_e \rangle} \left(\langle \mathbf{j} \rangle \cdot \nabla \left\langle \frac{\mathbf{j}_z}{\mathbf{n}_e} \right\rangle \right) + \frac{\mathbf{m}_e}{\langle \mathbf{n}_e \rangle e^2} \frac{\partial \langle \mathbf{j}_z \rangle}{\partial t} \\ & + \frac{-1}{\langle n_e \rangle} \langle \delta n_e \delta E_z \rangle + \frac{1}{e\langle n_e \rangle} \langle \delta \mathbf{j} \times \delta \mathbf{B} \rangle_z. \end{aligned} \quad (1)$$

In Eq. (1), $\frac{-1}{\langle n_e \rangle} \langle \delta n_e \delta E_z \rangle$ is the electrostatic (ES) turbulence contribution and $\frac{1}{e\langle n_e \rangle} \langle \delta \mathbf{j} \times \delta \mathbf{B} \rangle_z$ is the electromagnetic (EM) turbulence contribution to the reconnection field, while the first term is the Hall field, the second is the pressure gradient effect, and the third and the fourth are the electron inertial terms. In Figs. 3(c) and 3(d), the distributions of each of those terms and the reconnection electric field along the x direction are given at $t = 35T_0$ and $t = 50T_0$, respectively. It can be seen that both the electron pressure tensor gradient and ES turbulence dominate the reconnection process near the X point at $t = 50T_0$, different from previous studies in 3D reconnection where the EM turbulence plays an important role at the X point, while the ES turbulence contribution is very small [38,39]. This is due to the fact that the ultraintense lasers are injected continuously into the plasmas to generate intensive ES fluctuations propagating in the z direction, and the EM propagating operator in the general vorticity spreads the EM fluctuations out of the reconnection region.

A major consequence of reconnection is that the magnetic energy can be partially converted to particle kinetic energy. We then focus on the particle acceleration in the volume around the diffusion area, $10 \mu\text{m} < x < 14 \mu\text{m}$, $7 \mu\text{m} < y < 17 \mu\text{m}$, and $11 \mu\text{m} < z < 35 \mu\text{m}$ for MR at $t = 50T_0$. The distribution functions for the transverse and longitudinal momentum of the electrons and ions in this volume are then shown in Figs. 4(a)–4(f), respectively. In comparison with the single laser case (illustrated by red lines, without MR), clearly both electrons and ions are significantly accelerated in the MR process. For the single laser case the expansion of the bubble in the x direction can be seen in Fig. 4(b) for p_{ix} . Clearly, for the two laser case, ions are decelerated in the x direction in the selected box due to reconnection. On the other hand, electrons are still accelerated in the x direction though there should be a stagnation point of electron flow at the X point. This is due to the compressibility and z -direction acceleration of the electrons, and might be a reason why the reconnection rate is much higher than that of 2D MHD cases. For the longitudinal momentum p_z , more electrons are accelerated towards the $-z$ direction than that in the single laser case, while protons are accelerated in the $+z$ direction, due to the induced E_z field, as shown in Fig. 3. In the outflow directions, however, from

Figs. 4(c) and 4(d), it is found that both ions and electrons are accelerated substantially. It is shown clearly that a great portion of high energy protons are ejected to both sides together with peaks at $\pm V_A$ [Fig. 4(d)], with $p_{iy} \approx \pm 0.04$ [Fig. 4(d)].

In Fig. 4(g), the energy spectra of out-of-plane electrons and ions are shown at $t = 50T_0$ in the diffusion region around the X -point region. With reconnection, the electron spectrum clearly shows a collective acceleration by a $\Delta\gamma \sim 20$ –50 almost throughout the spectrum, corresponding to an energy gain of MeV level. It can also be seen in Fig. 4(c) that the electron momentum p_{ey} in the reconnection outflow direction approximately peaks at ± 50 . Therefore, our results provide evidence of particle acceleration and ultrahigh energy electron generation by magnetic reconnection in the X -point region in intense laser generated plasmas.

In summary, fast magnetic reconnection driven by two intense femtosecond lasers is studied by a self-consistent 3D relativistic PIC simulation. Magnetic reconnection geometry is built up while two identical intense laser pulses propagate in a near-critical density plasma. Evolution of the topological structure of magnetic reconnection is plotted to reveal the magnetic X -point in plane (of reconnection) and the out-of-plane quadrupole magnetic field component. The reconnection rate is calculated as $c\langle E_z \rangle / \langle B_A V_{Ae} \rangle = 0.44$ scaled by the electron Alfvén velocity instead of the Alfvén velocity. By the initial driven laser field E_0 , the reconnection rate can be scaled as $\langle E_z \rangle = 0.036$, larger than that previously obtained in two-fluid models. It shows clearly the strong driven and 3D reconnection features. Investigating the generalized Ohm's law, we find that the electron pressure tensor gradient and electrostatic turbulence terms dominate the reconnection process. By analyzing momentum distributions for electrons and ions in the reconnection area, both of them are accelerated in the reconnection outflow directions. For the longitudinal direction, electrons are accelerated backward while ions are accelerated forward by the induced reconnection electric field. Moreover, the energy spectra of electrons show ultrahighly energetic electron acceleration by an energy gain of MeV with $\Delta\gamma \sim 20$ –50. It may provide new mechanisms for some explosive astrophysical phenomena.

J.Y.Z. and Y.L.P. acknowledge the support of the K. C. Wong Education Foundation. The authors are grateful to Dr. H. Ji of PPPL for helpful discussions. This work was supported by the National Basic Research Program of China (Grants No. 2013CBA01502, No. 2013CBA01503, and No. 2013CBA01504) and by the National Natural Science Foundation of China (Grants No. 10905004, No. 11135012, No. 11121504, No. 11273033, No. 11220101002, No. 11261140326, and No. 10925421). Computer runs were performed on the Laohu high performance computer cluster of the National Astronomical Observatories, Chinese Academy of Sciences (NAOC).

[1] M. Yamada, R. Kulsrud, and H. Ji, *Rev. Mod. Phys.* **82**, 603 (2010).

[2] D. Biskamp, *Magnetic Reconnection in Plasmas* (Cambridge University Press, Cambridge, England, 2000).

[3] P. A. Sweet, in *The Neutral Point Theory of Solar Flares*, edited by B. Lehnert, IAU Symposia 6 (Cambridge University Press, Cambridge, England, 1958), p. 123.

[4] E. N. Parker, *Geophys. Res.* **62**, 509 (1957).

- [5] P. Brady, T. Ditmire, W. Horton, M. L. Mays, and Y. Zakharov, *Phys. Plasmas* **16**, 043112 (2009).
- [6] J. Goodman and D. Uzdensky, *Astrophys. J.* **688**, 555 (2008).
- [7] J. B. Taylor, *Rev. Mod. Phys.* **58**, 741 (1986).
- [8] R. P. Lin *et al.*, *Astrophys. J.* **595**, L69 (2003).
- [9] Yu. E. Lyubarskii, *Astron. Astrophys.* **308**, 809 (1996); Y. Lyubarsky and J. G. Kirk, *Astrophys. J.* **547**, 437 (2001); J. G. Kirk and O. Skjraasen, *ibid.* **591**, 366 (2003).
- [10] G. Drenkhahn, *Astron. Astrophys.* **387**, 714 (2002); B. Zhang, and H. Yan, *Astrophys. J.* **726**, 90 (2011); J. C. McKinney and D. A. Uzdensky, *Mon. Not. R. Astron. Soc.* **419**, 573 (2012).
- [11] T. Di Matteo, *Mon. Not. R. Astron. Soc.* **299**, L15 (1998); G. T. Birk, A. R. Crusius-Waetzell, and H. Lesch, *Astrophys. J.* **559**, 96 (2001).
- [12] P. M. Nilson *et al.*, *Phys. Rev. Lett.* **97**, 255001 (2006).
- [13] P. M. Nilson *et al.*, *Phys. Plasmas* **15**, 092701 (2008).
- [14] C. K. Li, C. K. Li, F. H. Séguin, J. A. Frenje, J. R. Rygg, R. D. Petrasso, R. P. J. Town, O. L. Landen, J. P. Knauer, and V. A. Smalyuk, *Phys. Rev. Lett.* **99**, 055001 (2007).
- [15] J. Zhong *et al.*, *Nat. Phys.* **6**, 984 (2010).
- [16] W. Fox, A. Bhattacharjee, and K. Germaschewski, *Phys. Rev. Lett.* **106**, 215003 (2011).
- [17] A. Pukhov and J. Meyer-ter-Vehn, *Phys. Rev. Lett.* **76**, 3975 (1996).
- [18] J. Fuchs, G. Malka, J. C. Adam *et al.*, *Phys. Rev. Lett.* **80**, 1658 (1998).
- [19] M. Tanimoto, S. Kato, E. Miura, N. Saito, K. Koyama, and J. K. Koga, *Phys. Rev. E* **68**, 026401 (2003).
- [20] Xian-Tu He, *Acta Phys. Sin.* **32**, 325 (1983) (in Chinese).
- [21] Z. M. Sheng and J. Meyer-ter-Vehn, *Phys. Rev. E* **54**, 1833 (1996).
- [22] B. Qiao, S.-p. Zhu, C. Y. Zheng, and X. T. He, *Phys. Plasmas* **12**, 053104 (2005).
- [23] U. Wagner *et al.*, *Phys. Rev. E* **70**, 026401 (2004).
- [24] G. A. Askar'yan *et al.*, *JETP Lett.* **60**, 251 (1994).
- [25] G. A. Askar'yan *et al.*, *Comments Plasma Phys. Controlled Fusion* **17**, 35 (1995).
- [26] M. Chen *et al.*, *Chin. J. Comput. Phys.* **25**, 43 (2008); X. Q. Yan, C. Lin, Z. M. Sheng, Z. Y. Guo, B. C. Liu, Y. R. Lu, J. X. Fang, and J. E. Chen, *Phys. Rev. Lett.* **100**, 135003 (2008).
- [27] B. Liu, H. Y. Wang, J. Liu, L. B. Fu, Y. J. Xu, X. Q. Yan, and X. T. He, *Phys. Rev. Lett.* **110**, 045002 (2013).
- [28] H. Shiraga *et al.*, *Plasma Phys. Control. Fusion* **53**, 124029 (2011).
- [29] J.-C. Gauthier, B. Hammel, H. Azechi, and C. Labaune, *J. Phys. IV France* **133**, V-6 (2006).
- [30] T. Nakamura, S. V. Bulanov, T. Z. Esirkepov, and M. Kando, *Phys. Rev. Lett.* **105**, 135002 (2010).
- [31] S. S. Bulanov *et al.*, *Phys. Plasmas* **17**, 043105 (2010).
- [32] A. Pukhov, Z. M. Sheng, and J. Meyer-ter-Vehn, *Phys. Plasmas* **6**, 2847 (1999).
- [33] Z. M. Sheng, K. Mima, Y. Sentoku, M. S. Jovanovic, T. Taguchi, J. Zhang, and J. Meyer-ter-Vehn, *Phys. Rev. Lett.* **88**, 055004 (2002).
- [34] J. Nycander and M. B. Isichenko, *Phys. Fluids B* **2**, 2042 (1990); S. K. Yadav, A. Das, and P. Kaw, *Phys. Plasmas* **15**, 062308 (2008).
- [35] M. Yamada, *Phys. Plasmas* **14**, 058102 (2007).
- [36] S. V. Bulanov, F. Pegoraro, and A. S. Sakharov, *Phys. Fluids B* **4**, 2499 (1992); L. C. Steinhauer and A. Ishida, *Phys. Plasmas* **5**, 2609 (1998); S. V. Bulanov, T. Zh. Esirkepov, D. Habs, F. Pegoraro, and T. Tajima, *Eur. Phys. J. D* **55**, 483 (2009).
- [37] J. D. Huba and L. I. Rudakov, *Phys. Rev. Lett.* **93**, 175003 (2004).
- [38] H. Che, J. F. Drake, and M. Swisdak, *Nature (London)* **474**, 184 (2011).
- [39] Keizo Fujimoto and Richard D. Sydora, *Phys. Rev. Lett.* **109**, 265004 (2012).